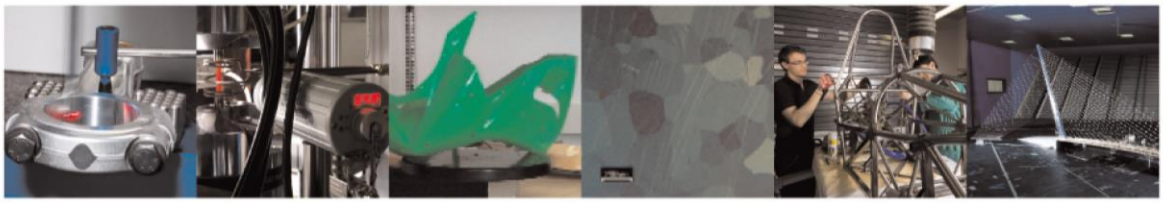

Laser surface texturing of ß-Ti alloy for orthopaedics: Effect of different wavelengths and pulse durations

Menci, G.; Demir, A. G.; Waugh, D. G.; Lawrence, J.; Previtali, B.

This is a post-peer-review, pre-copyedit version of an article published in APPLIED SURFACE SCIENCE. The final authenticated version is available online at:
http://dx.doi.org/10.1016/10.1016/j.apsusc.2019.05.111

DIPARTIMENTO DI MECCANICA ■ POLITECNICO DI MILANO
via G. La Masa, 1 ■ 20156 Milano ■ EMAIL (PEC): pecmecc@cert.polimi.it
http://www.mecc.polimi.it
Rev. 0

Laser surface texturing of β-Ti alloy for orthopaedics: Effect of different wavelengths and pulse durations

Giordano Menci[1], Ali Gökhan Demir[1,*], David G. Waugh[2], Jonathan Lawrence[2], Barbara Previtali[1]

[1]Department of Mechanical Engineering, Politecnico di Milano, Via La Masa 1, 20156 Milan, Italy

[2]School of Mechanical, Aerospace and Automotive Engineering, Faculty of Engineering, Environment and Computing, Coventry University, Gulson Road, Coventry, CV1 2JH, UK

*Corresponding author: aligokhan.demir@polimi.it

Laser surface texturing of β-Ti alloy for orthopaedics: Effect of different wavelengths and pulse durations

Giordano Menci[1], Ali Gökhan Demir[1,*], David G. Waugh[2], Jonathan Lawrence[2], Barbara Previtali[1]

[1]Department of Mechanical Engineering, Politecnico di Milano, Via La Masa 1, 20156 Milan, Italy

[2]Laser Engineering and Manufacturing Research Centre, University of Chester, Parkgate Road, Chester, CH1 4BJ, UK.

*Corresponding author: aligokhan.demir@polimi.it

Abstract

In this work laser surface texturing of Ti-11.5Mo-6Zr-4.5Sn β-Ti alloy is investigated with different laser wavelengths and pulse durations. For benchmark purposes three different industrial solid-state laser sources providing four different wavelength/pulse duration combinations were used. Within the experimented range pulse duration could be varied at 2.5 ps, 6 ns and 250 ns at 1064 nm, while 5 ns pulse duration was tested at 355 nm. The comparative analyses were carried within the process parameter ranges available to the laser sources in order to assess quality and productivity aspects. In particular, surface roughness, wettability and chemical composition were quantified as well as assessing the distinct surface morphologies obtained with different configurations. Process productivity was analysed for each configuration in terms of machining rate. The results exhibit a large variety of possible surface textures available to biomedical implant designers with naonmetric to micrometric features and tailorable chemical and wetting properties. Moreover, the results help understanding how the light/matter interaction changes between different pulse durations and wavelengths.

Keywords: Surface roughness; wettability; super hydrophilicity; laser induced periodic structures; ultrafast laser; UV laser

1. Introduction

Some of the desirable properties required in hip replacements are high biocompatibility, excellent mechanical properties like hardness, static and fatigue strength, thermal conductivity, low friction and mechanical shock resistance. Metallic implants all share these properties making them the most used material type for joint replacements [1]. When designing biomedical implants two main categories of properties should be taken into consideration: i) surface properties that affect bio-integration; and ii) bulk properties that meet the mechanical

requirements. The most common reasons for the failure of hip replacements are aseptic loosening of implants, osteolysis, implant wear and infection [2]. The interaction between the implant material and the surrounding physiological environment is of high importance. Hence, both material choice and surface preparation play critical roles in the correct functioning of the biomedical implant.

The three most dominant metals used in joint replacements are AISI 316L stainless steel, cobalt-chrome alloys (Co-Cr) and titanium alloys (Ti-6Al-4V) [1,3]. All these alloys possess higher elastic modulus than bone, leading to insufficient stress transfer to bone and promoting bone resorption and loosening of the implant after some years of implantation. Among these metallic materials, titanium and its alloys are favorable to other orthopedic implant materials due to their high specific strength and fatigue resistance, excellent biocompatibility properties, and good corrosion resistance [4–7]. Commercially pure (cp) Ti and Ti-6Al-4V are the most commonly used titanium alloys for endosseous implant applications. The high elastic modulus remains an important limitation on the performance of Ti alloys as implant materials for artificial joints (e.g. hip, knee or shoulder joints, *etc*). It is essential that the stiffness of the implanted material is as close as possible to the connected bone. This characteristic facilitates an effective transfer of mechanical stress, by providing stress shielding effect [2,8]. Ti-6Al-4V alloy has a modulus of approximately 110 GPa [9], which is extensively higher than that of human bone (10- 40 GPa) [2]. The high modulus of Ti-6Al-4V is correlated to the high amount of Al content which leads to increase in volume fraction of α phase [2]; moreover, the long-term performance of Ti-6Al-4V alloy has raised some concerns due to the release of aluminium and vanadium.

Beta titanium alloys form one of the most versatile classes of materials with respect to processing, microstructure, and mechanical properties. Recently, β-type Ti alloys containing Nb, Zr, Ta, Mo, Sn, just to mention a few, have attracted considerable attention especially for orthopaedic implants applications owing to their unique combination of better mechanical properties, low elastic modulus, superior biocorrosion resistance, no allergic problems, and excellent biocompatibility. It has been found that their elastic modulus can be significantly reduced by adjusting the concentration of β stabilizing elements [10].

While initial chemical composition, subsequent manufacturing processes and final post-treatment procedures define the bulk properties of Ti-based implants, surface treatments and texturing determine the interaction with tissue and bones. In order to improve the implant-tissue interaction surface preparations are common to orthopedic implants. Laser surface texturing is a less-explored option in terms of industrial use, despite several

intrinsic advantages such as non-contact interaction, environmentally friendly processing conditions, high repeatability and flexibility and the possibility to generate both deterministic and stochastic surface structures through a digital manufacturing environment [11–13]. The main issue lies over the fact that several laser sources are available, which can generate different surface structures. By properly selecting the laser processing parameters, the topography and chemistry of the implant surfaces can be optimized for the desired biomedical application. Hence, an aid to assess these parameters and allocate them on the implant surface is essentially required.

Laser surface texturing allows fabricating implants with enhanced biological response characteristics, in which laser-induced surface textures are employed to control protein adsorption and cell adhesion [14–17]. The process produces minimal contamination compared to conventional surface modification techniques, thus it can help improve osseointegration [18–20]. The highest implant stability can be achieved by complete osseointegration of a large implant surface. Several publications have shown that roughness and wettability produced by laser modification plays a vital role in biocompatibility properties [21–25]. Hao *et al.* [25] showed that improved surface roughness, surface oxygen content and surface energy generated by laser treatment accounted for the better wettability characteristics of the material and enhancement of the adhesion with the biological liquids used. Furthermore, an investigation of initial cell spreading and adhesion on longitudinally and transversally oriented micro-grooves produced by the laser irradiation of Ti-6Al-4V surfaces was carried out by J. Chen *et al.* [26]. Results of the experiment showed that cell spreading and adhesion were enhanced by the longitudinally and transversally oriented microgrooves. Contact guidance was found to promote cell adhesion due to the increase in interactions between the focal adhesions and the patterned extra-cellular matrix (ECM) proteins on the laser micro-grooved surfaces [26].

Ansalme *et al.* [27] found that rougher titanium implants have stronger bone response compared to smoother implants after a long term implantation. A study conducted by Hallgren *et al.* [28] showed that the periodic arrays of micron-sized craters on dental implants improves dental tissue growth and implant stability. Several other studies showed various surface topographies generated by laser machining to improve cell adhesion on Ti-alloys [29–31].

The most common form of surface morphologies are based on micropits, grooves or a chaotic surface structure in order to provide a general increase of surface roughness. The used laser sources implemented vary from fs-

pulsed to ns-pulsed to continuous wave, as well as wavelengths from ultraviolet (UV) to infrared (IR). It is well-known to the laser-based manufacturing community that ultrashort pulsed lasers(from fs to ps) can provide cold ablation, while longer pulses (ns) can induce melt formation and vaporization, which can be exploited differently [32–34].

A comprehensive study on the differences of using different pulse durations and wavelengths for obtaining different surface structures is missing from the literature. From the point of view of authors, β -Ti alloys seem to have been neglected completely. Evidently, the laser process can provide benefits by improving the surface texture for the application, while it can also induce excessive surface oxidation and thermal damage. Such conditions require further attention for β-Ti alloys to avoid α-phase formation. Before the extensive biological studies, the possibilities in terms of topological and chemical modifications should be carefully studied. Therefore, in this work laser surface texturing of Ti-11.5Mo-6Zr-4.5Sn β-Ti alloy is investigated employing 4 different solid state lasers based on Nd:YAG and fiber architectures providing ps to ns pulse durations and UV to near infrared (NIR) wavelengths. Results are analysed in terms of surface morphology, wettability characteristics and surface chemistry. Ordered structures, chaotic patterns as well as laser induced periodic structures (LIPSS) are demonstrated by exploiting the different pulse durations, wavelengths as well as pulse repetition rates. The possibility of using different surface textures on different parts of hip implants as well as manufacturing productivity concerns are discussed.

2. Surface requirements of an orthopaedic implant

A typical femoral component of a total hip replacement implant is composed of the femoral head, the femoral stem and the acetabular cup. A β-Ti implant provides a more desirable elastic modulus, on which different surface textures could be employed to tailor the properties locally. The acetabular cup and the femoral stem are expected to provide good osseointegration, and so high surface roughness and low surface wettability are desirable. From this point of view, the highly rough and hydrophilic surfaces can be useful. Excessive thermal damage can lead to and increase the α-phase content and potentially increase the elastic modulus. Excessive oxidation can also be detrimental for the mechanical properties due to the induced fragility. LIPSS have shown to be favourable for reducing friction and wear [35], which can be exploited on the femoral head. Moreover, it has been shown that such surfaces can provide antibacterial properties [36], and can be exploited also on the

femoral stem, which has a large contact area with the bone. The work assesses the capability of four different laser systems in providing the required surface structures, while assessing their productivity as well.

3. Materials and methods

3.1. Material

Cold-rolled, 0.42 mm-thick sheets of titanium β III alloy (Ti-11.5Mo-6Zr-4.5Sn) were used throughout the study (Goodfellow, Cambridge, UK). The alloy possesses a nominal compressive yield strength of 800 MPa and an elastic modulus of 79 GPa. Table 1 reports the nominal chemical composition of the alloy. Average surface roughness of the as-received samples was Sa=0.38± 0.03 μm, whereas the average water contact angle was measured at 61°± 5°. Figure 1 shows the scanning electron microscope (SEM) image of the as-received sample surface.

Table 1. The nominal chemical composition of the titanium β III alloy .

Element	Mo	Zr	Sn	Fe	C	N	H	O	Ti
wt.%	11.5	6.0	4.5	≤0.35	≤0.10	≤0.05	≤0.02	≤0.18	bal.

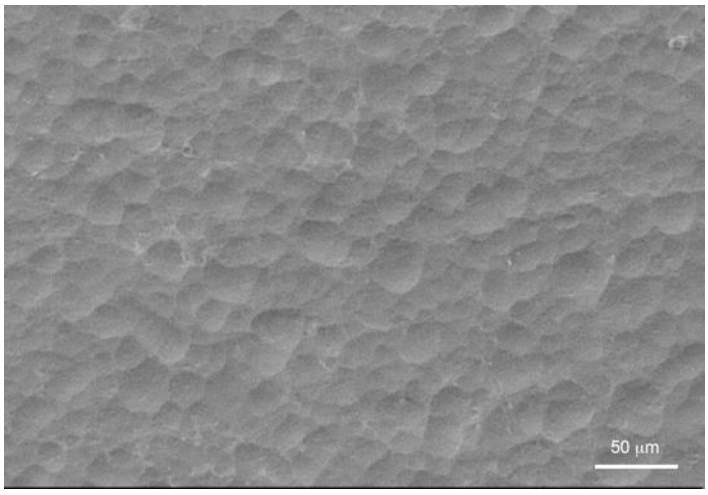

Figure 1. SEM image of the as received surface of the β-Ti alloy.

3.2. Laser systems

Three different laser systems were employed in the study providing pulse durations from ps to ns range with wavelengths from UV to near-IR (see Table 2). Two of the employed sources were based on active fiber laser

technology providing ps and ns pulses with high repetition rates. The ultrashort pulsed laser (Fianium HE 1060 from NKT Photonics, Birkerød, Denmark) was based on a passively mode-locked fiber oscillator and fiber amplifier. The laser provided pulse durations of approximately 2.5 ps with 1064 nm of emission wavelength with pulse repetition up to 500 kHz and pulse energy up to 10 μJ. The sub-microsecond fiber laser (YLP 1/100/50/50 from IPG Photonics, Cambridge, MA, USA) was Q-switched producing pulses of 250 ns duration at 1064 nm emission wavelength. The laser produced pulse energy up to 1020 μJ with pulse repetition rates between 20-50 kHz. Both the fiber lasers were coupled to scanner heads exploiting the high repetition rates available with high scan speeds. F-theta lenses with 160 mm (Miniscan II from, Raylase, Weßling, Germany) and 100 mm (TSH 8310 from Century Sunny, Beijing, China) focal lengths were couple to ps-pulsed fiber and ns-pulsed fiber lasers respectively. A diode pumped Nd:YAG laser (Quantel 850 from Lumibird, Lannion, France) was used producing approximately 5 ns pulse duration with a fundamental wavelength at 1064 nm producing pulse energy levels up to 825 mJ. The same laser could be used with the integrated third harmonic generator emitting at 355 nm with pulse energy up to 225 mJ. The energy of the laser beam was reduced by means of a spatial filter for both the wavelengths. Then, the laser beam was focused with a 100 mm focal lens and the workpiece was moved via linear stages (ILS150 from Newport, Irvine, CA, USA). System configurations are schematically shown in Figure 2 and the main parameters of the laser systems is given in Table 2.

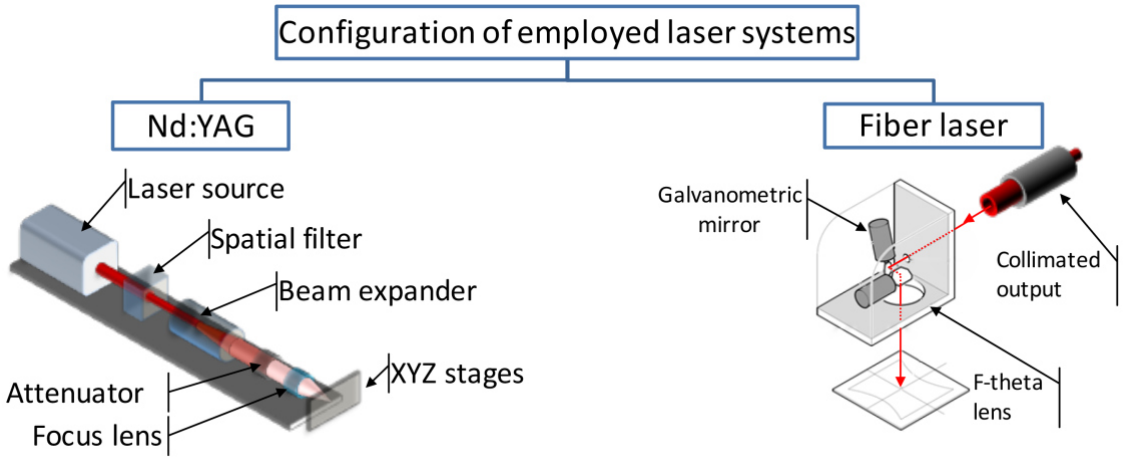

Figure 2. Schematic representation of the different configurations used in the experimental study.

Table 2. Main characteristics of the employed laser systems.

Laser source	Fiber, ps, 1064 nm	Nd:YAG, ns, 355 nm	Nd:YAG, ns, 1064 nm	Fiber, ns, 1064 nm
Pulse duration, τ	2,5 ps	5 ns	6 ns	250 ns
Pulse energy, E	0.1 – 8 µJ	700-2600 µJ	400 – 900 µJ	42 – 1020 µJ
Pulse repetition rate, PRR	Single pulse to 500 kHz	10 Hz	10 Hz	20 – 80 kHz
Beam quality factor, M^2	1.3	≤2	≤2	1.7
Max. peak power, P_{peak}	3760 kW*	407 kW*	170 kW*	9 kW
Beam positioning	Scanner head	Linear stages	Linear stages	Scanner
Focal lens, f	160 mm	100 mm	100 mm	100 mm
Focused beam diameter, d_0	34 µm	15 µm	19 µm	39 µm
Polarization state	Linear	Linear	Linear	Random

*Estimated for Gaussian pulse shape.

3.3. Material analysis

Prior to characterization all samples were cleaned ethanol in ultrasonic bath for 15 minutes and dried in open air. Images were acquired of all the laser textured specimens using a scanning electron microscope (SEM) (EVO-50 from Carl Zeiss, Oberkochen, Germany). Surface roughness was measured by confocal microscopy (MarSurf CWM100 from Mahr, Göttingen, Germany). Acquisitions were made over area of 192x144 μm^2 with 100X lens. Estimated lateral and axial resolutions were 0.25 µm and 1 µm respectively. Surface wettability was measured with a sessile drop system (OCA20 from Dataphysics Instruments, GmbH, Germany). Distilled water was used as testing media. A wait period of 30 seconds was used before each measurement of contact angle to ensure that the droplet was in equilibrium. X-ray diffraction (XRD) patterns of the representative samples were recorded using a system with Cu Kα (λ = 1.5418 Å) radiation (D8 XRD from Bruker, UK). X-ray photoelectron spectroscopy (XPS) was also used on selected conditions (Phoibos 150 from Specs Gmbh, Berlin, Germany). Spectra were quantified using dedicated software (CasaXPS v2.3.16, Casa Software, Teignmouth, UK) and Scofiled cross-sections corrected for the energy dependence of the instrument transmission and the effective electron attenuation lengths.

3.4. Experimental plan

Laser surface texturing was applied with a common scan strategy consisting of overlapped pulses over linear tracks with a certain distance. The main control parameters are laser pulse energy, *E*, pulse repetition rate, *PRR*, and pitch, *p* between adjacent scan lines. The laser configurations are characterized by high *PRR* with a scanner (Fiber, ps, 1064 nm; Fiber, ns, 1064 nm) and low *PRR* with linear stages (Nd:YAG, ns, 355 nm; Nd:YAG, ns, 1064 nm). Also, the beam diameters differed between laser systems. As depicted in Figure 3, over a single scan an increase in scan speed resulted in a decreased overlap. The different laser sources and employed beam positioning systems require different scan speed levels. To maintain similar levels of pulse overlap, the processing conditions should be specific with regard to the scan speed and pitch. Overlap on the scan direction, O_x, can be calculated by:

$$O_x = 1 - \frac{v}{PRR \cdot d_0} \quad (1)$$

where d_0 is the beam diameter. It can be seen that the difference between the high *PRR* and low *PRR* systems need to be contrasted by lowering the scan speed. The overlap between the consecutive scan lines, O_y, can be expressed by:

$$O_y = 1 - \frac{p}{d_0} \quad (2)$$

The pitch and beam diameter control the overlap between the scan lines. A negative value of this parameter represents complete separation between adjacent lines. It should be noted that the beam size, incident on the material surface, is used to estimate the overlap as the final extent of the processed line depends on the ablated region's extent [37]. Due to this fact, each laser system configuration levels were set separately in order to avoid parameter sets that are not sufficient to produce any relevant surface texture and achieve comparable conditions in terms of pulse overlap over the scanned line and between adjacent lines. The levels were set after preliminary experiments, which are not reported here for brevity. On the other hand, the same experimental design was set for each laser system configuration. Pulse energy, scan speed and pitch were varied at 3, 2 and 3 levels respectively. Pulse repetition rate was fixed at different levels for all configurations. All experiments were carried out with the focal plane over the material surface and in ambient atmosphere. Table 3 reports the details of the executed experimental plan. Table 4 and Table 5 report the calculated overlap values for all the tested parameter sets.

Each tested combination was analysed with SEM. Surface profiles were acquired with confocal microscopy at three distinct positions of the specimen. Contact angle measurements were done on each sample. Four

measurements were taken and averaged. For each laser configuration highest and lowest roughness conditions as well as conditions with highest and lowest contact angle were chosen for further XRD analyses.

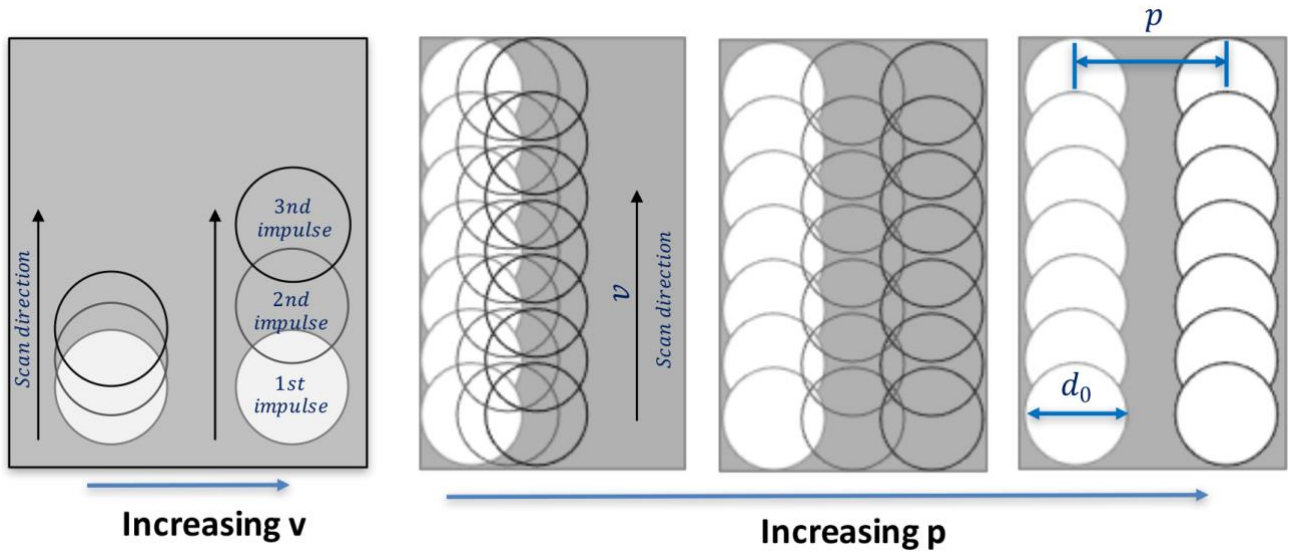

Figure 3. Effect of scan speed (v) and pitch (p) over pulse overlap over the single scan track and adjacent tracks.

Table 3. Details of the experimental conditions for each laser configuration.

Laser source	**Fiber, ps, 1064 nm**	**Nd:YAG, ns, 355 nm**	**Nd:YAG, ns, 1064 nm**	**Fiber, ns, 1064 nm**
Fixed Parameters				
Focal position, Δz	0 mm	0 mm	0 mm	0 mm
Pulse repetition rate	50 kHz	10 Hz	10 Hz	50 kHz
Varied Parameters				
Pulse Energy, E (µJ)	4; 6; 8	720; 1470; 2040	440; 670; 730	129; 364; 600
Scan speed, v (mm/s)	172; 345	0.05; 0.15	0.07; 0.21	340; 1020
Pitch, p (µm)	14; 28; 52	14; 28; 52	10; 20; 38	14; 28; 52

Table 4. Calculated overlap along the scan direction for the different parameter combinations.

Laser	**d_0 (µm)**	**PRR (Hz)**	**v (mm/s)**	**O_x**
Fiber, ps, 1064 nm	34	50000	172	0.90
			345	0.80
Nd:YAG, ns, 355 nm	15	10	0.05	0.67

			0.15	0.00
Nd:YAG, ns, 1064 nm	19	10	0.07	0.63
			0.21	-0.11
Fiber, ns, 1064 nm	39	50000	340	0.83
			1020	0.48

Table 5. Calculated overlap between the scan lines for the different parameter combinations.

Laser source	d_0 (µm)	p (µm)	O_y
Fiber, ps, 1064 nm	34	14	0.59
		28	0.18
		52	-0.53
Nd:YAG, ns, 355 nm	15	10	0.33
		20	-0.33
		38	-1.53
Nd:YAG, ns, 1064 nm	19	14	0.26
		28	-0.47
		52	-1.74
Fiber, ns, 1064 nm	39	14	0.64
		28	0.28
		52	-0.33

4. Results and discussion

4.1. Surface morphology

Figure 4 to Figure 7 show SEM images of the obtained surface structures as a function of process parameters. In Figure 4, it can be seen that the ps-pulsed laser generates the so called ripple or LIPSS. The smaller laser energy appeared to generate a well-defined and repetitive pattern. Kietzig *et al.* [38] showed that the use of high energy results in the generation of a coarser structure made of protrusions and a micro bumps along with the LIPSS. Pitch improved the surface coverage. The scan speed did not appear to provide a significant change in the surface morphology. Tanvir Ahmmed *et al.* [39] showed that pulse overlap required for the formation of coarser structures is much higher than the used values in this work. Concerning the ns-pulsed Nd:YAG UV laser, the images in Figure 5 show that all parameters induce significant changes in the surface morphology. The material removal mechanism appears to be composed of melt expulsion and evaporation. The expelled molten material forms ridges that contribute to a chain-like surface texture in a repetitive way. The overlapping

of the laser pulses is apparent at high pitch and conditions. Reduced pitch and scan speed generate a new surface texture that is predominantly following the scan direction with a more chaotic pattern. A similar trend is viewed for the ns-pulsed Nd:YAG laser with 1064 nm wavelength as seen in Figure 6.In this case, however, the chain-like surface structure remains visible in all parameter combinations. This is mainly due to the larger spot obtained in the optical configuration, which decreases the irradiance; hence the molten fraction is larger and the obtained surface texture is predominantly formed by the molten material movement. Finally, Figure 7 represents the obtained surfaces with the ns-pulsed fiber laser operating at 1064 nm wavelength. This options proves to be the most versatile in terms of the obtained textures. At low energy, high pitch and high speed conditions, which indeed involves the smallest amount of total energy released, the surface is composed of the chai-like structures. A decrease of the scan speed generates deeper grooves along the scan direction. Chaotic texture formation occurs in all low pitch conditions, as well as the high energy conditions with the higher pitch. The surface texture is then composed of small droplets of condensed material, which is a sign of explosive behavior during the process. During the solidification, often fractal forms appear generating a hierarchical nano- to micro-surface texture with a chaotic form [40,41]. Undercuts were also formed due to the violent melt flow during the process.

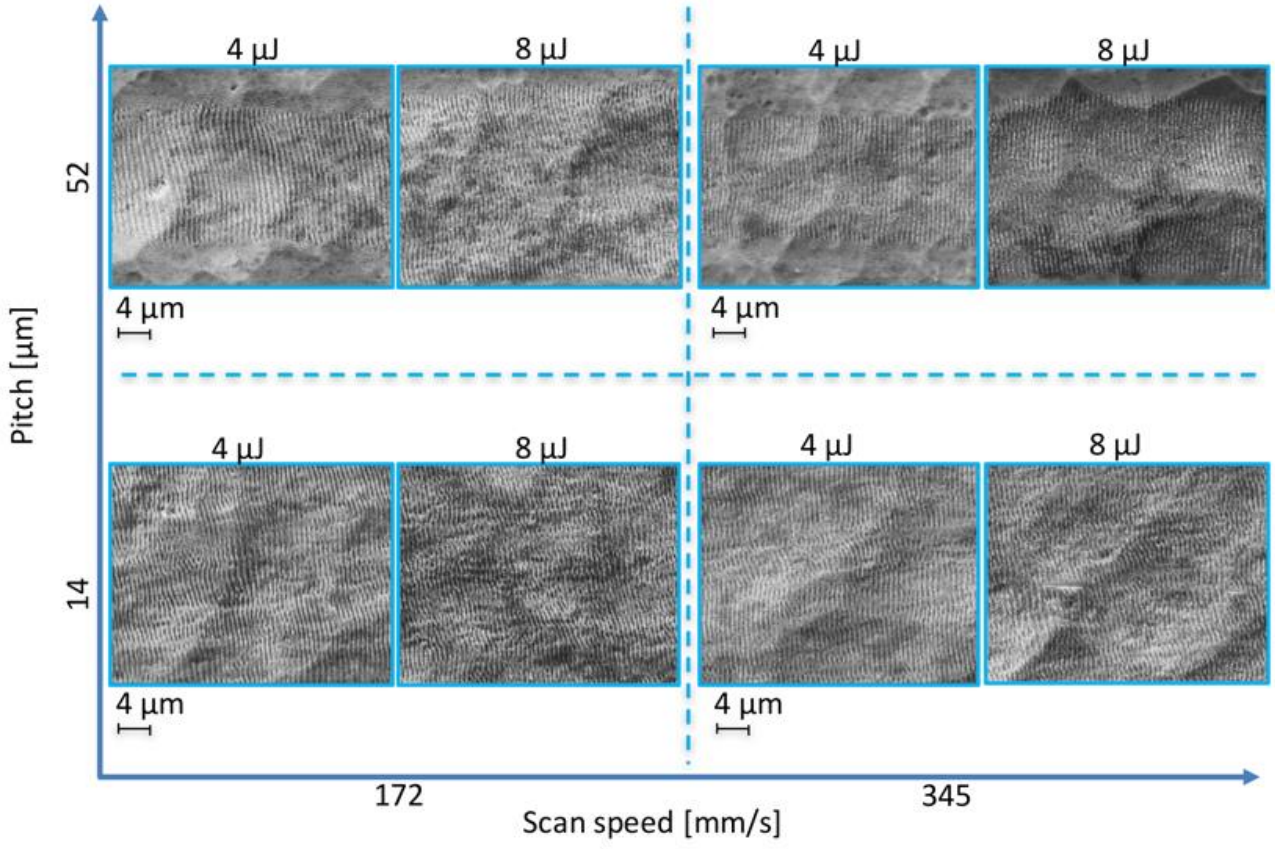

Figure 4. SEM images of the surfaces obtained as a function of process parameters with ps-pulsed fiber laser at 1064 nm.

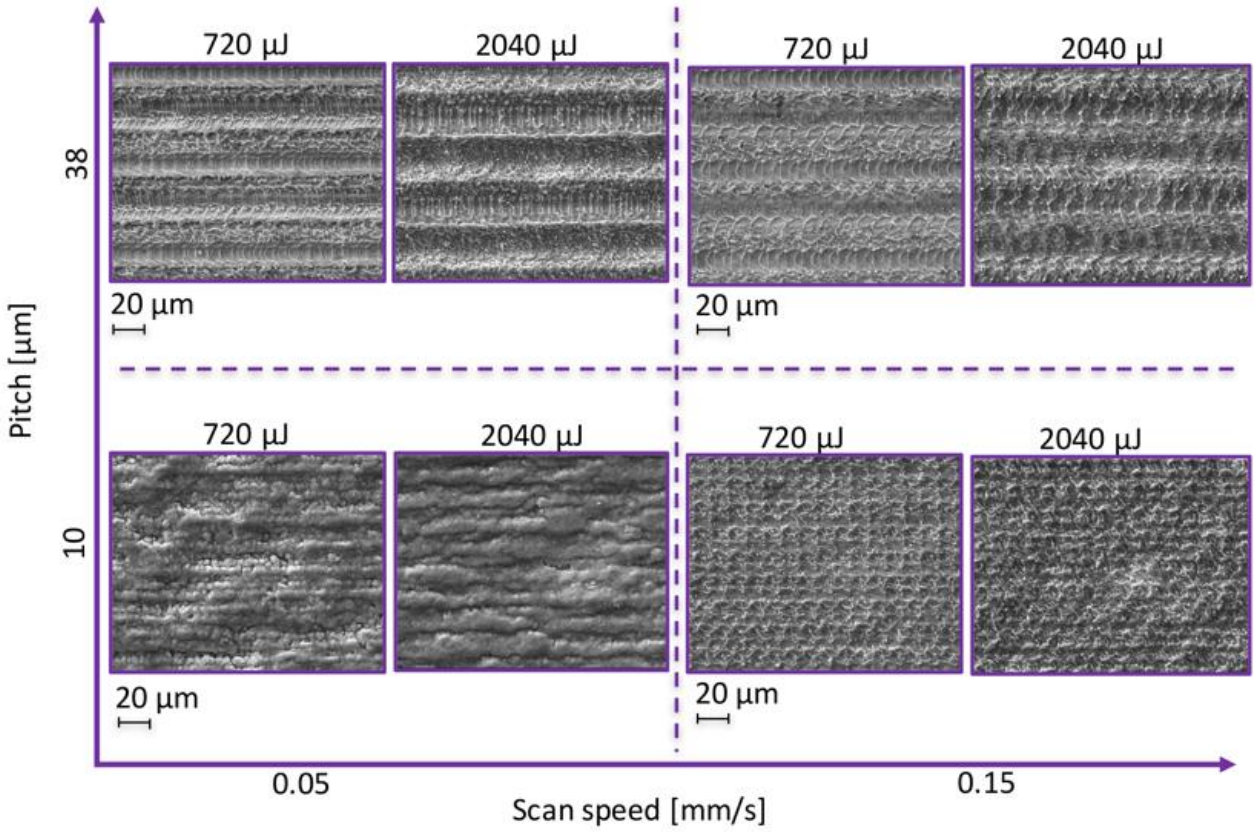

Figure 5. SEM images of the surfaces obtained as a function of process parameters with ns-pulsed Nd:YAG laser at 355 nm.

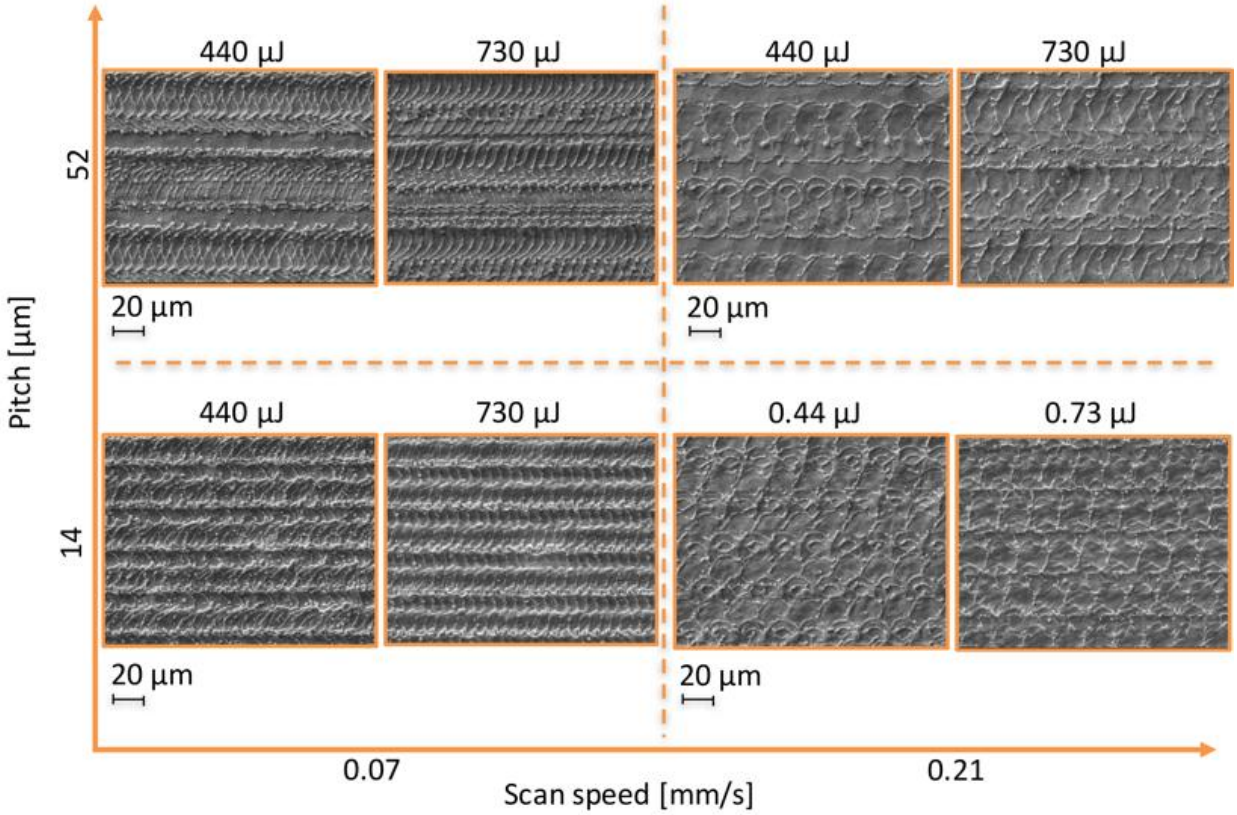

Figure 6. SEM images of the surfaces obtained as a function of process parameters with ns-pulsed Nd:YAG laser at 1064 nm.

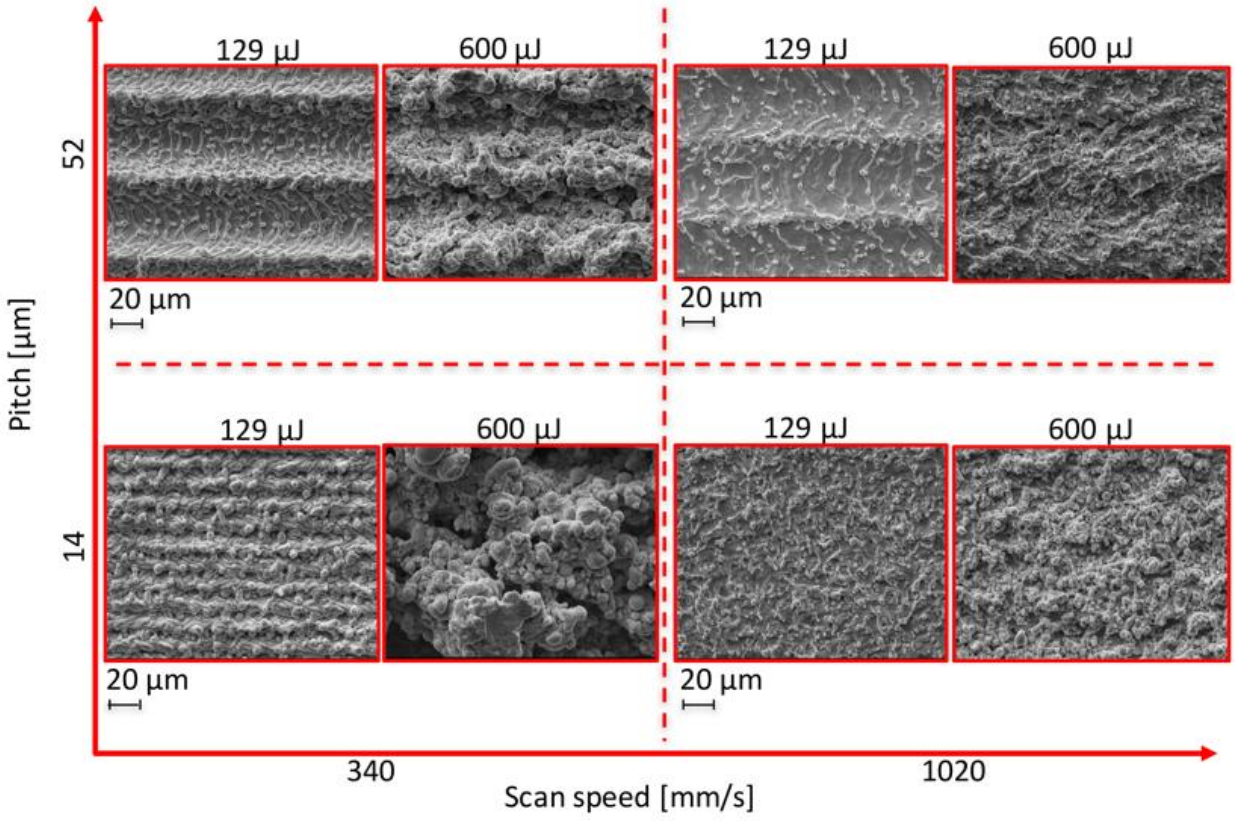

Figure 7. SEM images of the surfaces obtained as a function of process parameters with ns-pulsed fiber laser at 1064 nm.

The observed surface structures give insights to the differences in the light-material interaction. The first and the most obvious distinction is made between ps- and ns-pulsed processing. The interaction with ultrashort pulses is limited to the light absorption, which induces the cold-ablation phenomenon [32]. The LIPSS form under the polarized laser light due to the imperfect surface causing internal local reflections and hence interference phenomenon [42]. Due to the non-thermal interaction the sub-micrometrics structures survive the ablation process without being filled with molten material. If the process is maintained at cold ablation conditions without excessive heat build-up due to very low scan speeds or very high repetition rates, the surface can be filled with these structures.

The Nd:YAG sources also emit polarized light. However, the longer pulse duration causes the melt generation. Hence, LIPSS formation cannot be observed due to the refilling of the generated nanostructures with the melt flow. Ti-alloys are also known to be prone to dross-formation [43,44]. This combination results in a surface texture that is dominated by the molten material movement. The use of UV wavelength opposed to the NIR is mainly advantageous for a smaller beam and a higher irradiance. The ablated region was therefore smaller, and as the pitch and scan speed decrease the surface texture tended towards a grooved form. On the other hand, the ns-pulsed fiber laser with 1064 nm wavelength induces a rapid transformation between several surface textures. The main difference of this source to the Nd:YAG counterparts is the high repetition rate employed and the longer duration of the pulses. It has been shown that moving the pulse duration from the lower end (1-10 ns) to the higher end (>100 ns) of ns domain increased the melt fraction drastically [45,46]. Despite the high scan speeds employed, the high repetition rate of the pulses can induce a thermal accumulation. This generates a higher fraction of molten material as well as vapour. The vapour exerts pressure on the molten material to expel it violently causing the small fragments and droplets around the processing region. High surface to volume ratio of such particulate generates a fast cooling cycle leading into the chaotic texture forms [40]. Such chaotic textures were observed on an alpha-Ti alloy under multiple scan passes [47]. The average surface roughness of the ns-pulsed fiber laser treated conditions have a much larger extent approximately 1-15 µm approximately.

4.2. Surface roughness

Figure 8 shows the measured average surface roughness values. The contribution of the nanometric LIPSS to the average surface roughness is limited. Overall, a slight increase compared to the initial surface roughness

was achieved, while the process parameters do not provide a significant difference. This fact can be advantageous for a non-invasive surface treatment for the orthopaedic implants. The Nd:YAG laser sources show a similar behaviour in the increase of the average surface roughness as a function or process parameters. At low scan speeds, the surface roughness increased at highly energetic conditions. With the UV light sources the maximum Sa is higher at approximately 2 µm, concerning the conditions with high energy, low speed and low pitch. The grooved surface texture low pitch and low scan speed values provided average surface roughness between approximately 0.5-1 µm. Such conditions are exploitable for osteointegration without excessive damage on the component. As a matter of fact, the surface roughness values represent also transformation between different surface texture types from chain-like to chaotic compact to finally chaotic with undercuts. Despite the several implications of favourable use of chaotic surface texture with undercuts, the high surface roughness is also an indication to fragility and possibility of delamination. Moreover, the surface roughness measurements do not yield information concerning surface porosity, which may lead into lower wear resistance.

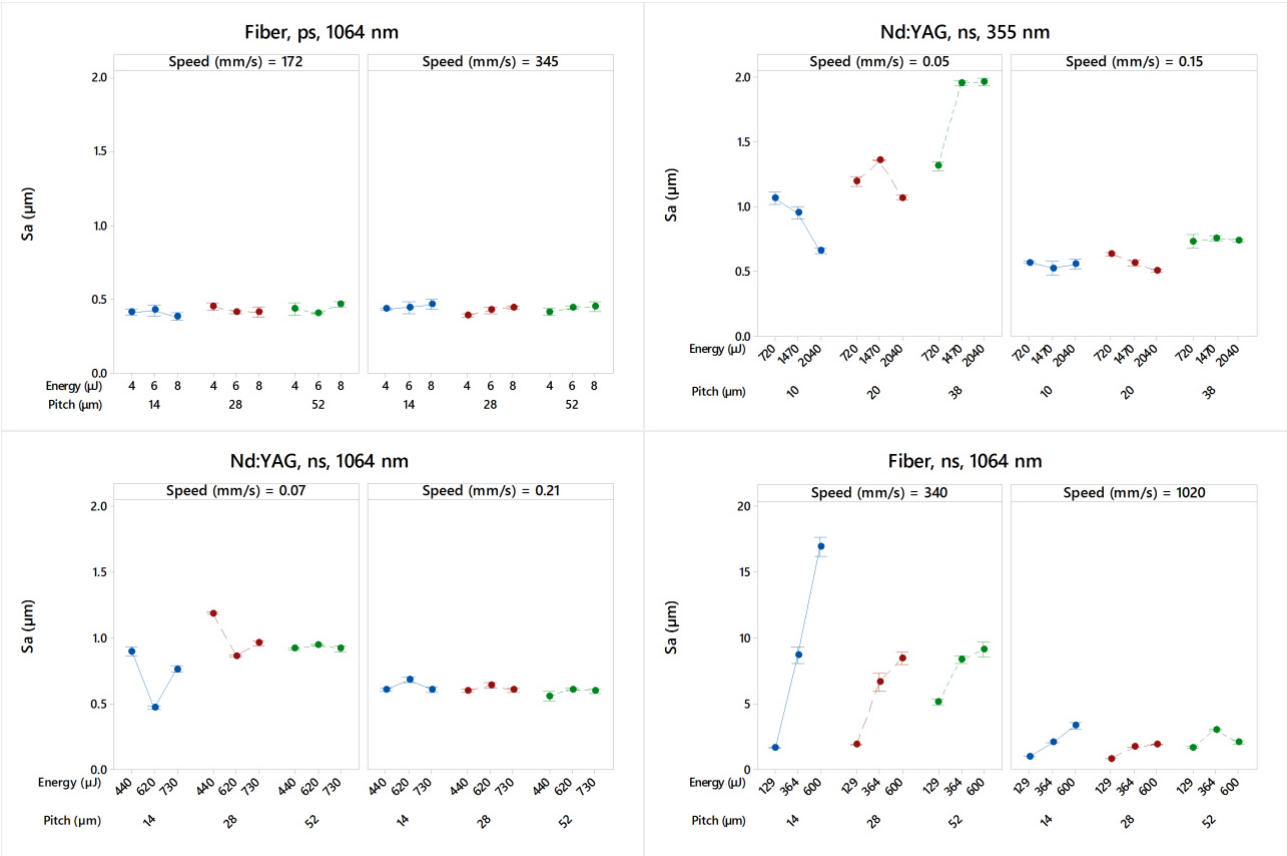

Figure 8. Average surface roughness (Sa) obtained as a function of process parameters and laser configurations. Note the different scale for the ns-pulsed fiber laser with 1064 nm wavelength, which is larger for readability.

4.3. Wettability

A direct link between the surface roughness and the water contact angle was sought for all the processed conditions. Figure 9 shows the water contact angle of all the processed surface with plotted against the average surface roughness. A non-linear decay is present for the conditions coming from ns-pulsed lasers. This is similar to the Wenzel behaviour, where an increase in the surface roughness results in a more hydrophilic behaviour. Wenzel defines that a relationship between the contact angle of ideally flat surface, θ_y, and the contact angle of rough surface, θ_w, exists with

$$\cos\theta_w = r\cos\theta_y \quad (3)$$

where r is the roughness factor, which is the ratio between effective surface area and an ideally flat surface area. As the surface roughness increases the surfaces tend to a superhydrophilic behaviour; however, this does not follow strictly Wenzel's equation. Cassie and Baxter introduced Indeed the gaseous phase in the liquid and surface interaction and expressed the contact angle behaviour with

$$\cos\theta_c = f\cos\theta_y - (1-f) \quad (4)$$

where f and $(1-f)$ are the area fractions of the solid and gas phases on the surface. According to Equation (4), the gaseous phase entrapment can increase the contact angle, even if the ideally flat surface is hydrophobic. It can ben deduced that the highly rough surfaces obtained in this work with the ns-pulsed fiber laser entrap also the gaseous phase that does not allow the rapid decrease of the water contact angle as expressed by Wenzel. Another important factor for reducing the contact angle is the change in the chemical composition of the surface. Such difference can be interpreted as a change in the equivalent contact angle of the ideally flat surface. During the processing in the ambient atmosphere surface oxidation is expected. The TiO_2 can be formed, which has high chemical reactivity with water [48]. This can contribute to the superhydrophilic behaviour.

On the other hand, the ps-pulsed laser produced a slight increase of water contact angle. This is an indicator to the switch towards a Cassie-Baxter type of surface behaviour. Such conditions may also be explained by a wetting transition and mixed-state phenomenon [49]. Indeed, LIPSS can be exploited to induce

superhydrophobicity [38]. It has been shown that such phenomenon may occur over time [38,50], which is referred to as hydrophobic recovery.

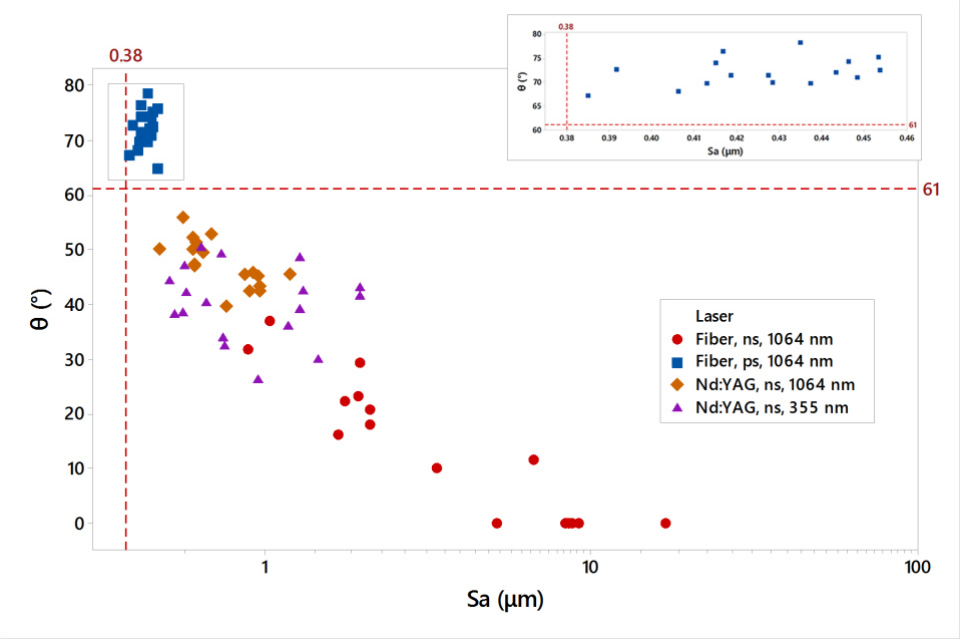

Figure 9. Surface wettability as a function of average surface roughness obtained with different laser configurations. Image inset shows the low roughness region (Sa=0.38-0.48 µm) belonging to the conditions obtained with ps-pulsed fiber laser at 1064 nm.

4.4. Surface chemistry

XRD spectra of representative process conditions are reported in Figure 10. For each laser source, surfaces with the lowest and highest average roughness, as well as the highest and lowest contact angles, were considered. The spectra were compared to the as-received sample condition. The ps-pulsed laser evidently shows no remarkable difference compared to the initial surface chemistry. For the ns-pulsed lasers the surface oxidation appeared to be present as TiO_2 peaks appear both in anatase and rutile form. Amorphous TiO_2 can form anatase crystal form by annealing around 300°C. Above 700°C anatase TiO_2 converts to rutile crystal [51]. When Ti and TiO_2 react at approximately, Ti_2O_3 forms 1600°C [52].

Weak anatase and rutile peaks formed with the Nd:YAG sources at 355 nm and 1064 nm. With the ns-pulsed fiber laser, stronger peaks are observed accompanied by the formation of Ti_2O_3 at the highest surface roughness condition, which also belongs to the most energetic process parameter set. This information when combined strengthens the observed wettability behaviour and the conclusions derived therefrom. The stronger surface oxidation is present with the most complex surface geometries on the ns-fiber laser textured surfaces; therefore,

a mixed behaviour of gas entrapment and affinity to oxygen is observed. TiO_2 can become highly hydrophilic upon irradiation with UV laser light. This is explained by photogeneration of holes, which are first produced in the bulk of TiO_2, then diffused to the surface and are trapped at lattice oxygen sites [51]. Such regions possess high affinity to the oxygen of water, which renders the surface superhydrophilic. The photogenerated holes are recovered once the surface is stored in darkness. The NIR wavelength of the ns-pulsed fiber laser is not expected to directly induce the required photochemical transition. Still, it has been observed that the rutile TiO_2 can be superhydrophilic right after its formation [48]. An indirect UV light source during the processing can be formed by the plasma emission, since Ti emission lines can be found around the UV region [53].

Another important phenomenon observed in the XRD spectra is the presence of α-Ti peaks in the conditions referring to ns-pulsed lasers. The α-phase can be formed in β-Ti alloys via heat treatment. Commonly, a solution treatment applied, which is followed by aging at temperatures of 450 to 650 °C to form finely dispersed α particles in the retained β [51]. Although the process durations are much shorter, it is expected that the high temperatures generated during the ablation process can result in a superficial modification of the alloy's crystallographic structure. Indeed, the formed oxides indicate temperatures that are higher than those for the aging treatment. Apparently, such formation is amplified towards more energetic conditions of the ns-pulsed fiber laser. It should be noted that the formation of the α-phase can be disadvantageous for the use of an orthopaedic implant. The lower elastic modulus of the β-alloys is compromised. In other cases, it can be used for local modifications of the mechanical properties of the component along with the surface texture.

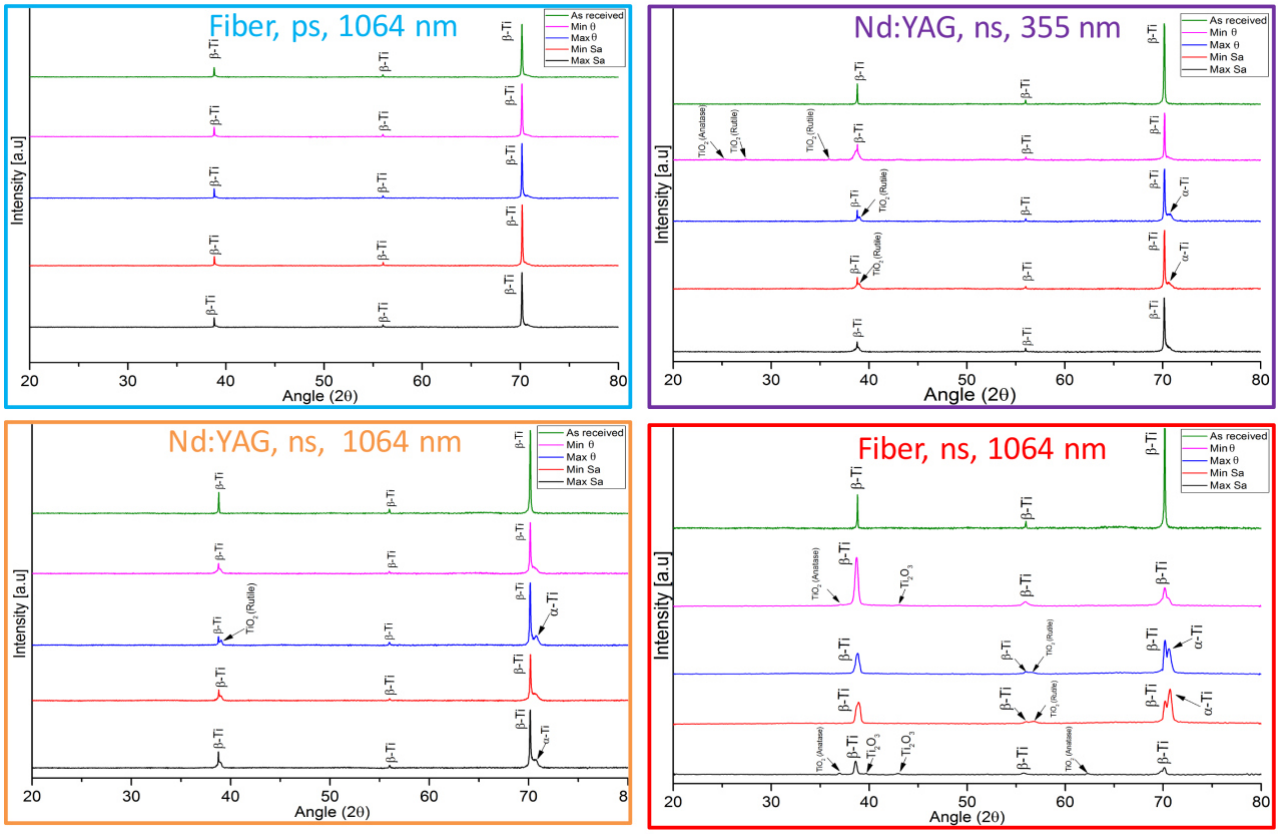

Figure 10. XRD analysis of the representative conditions obtained with each laser source.

Figure 11 shows the summary of atomic concentrations revealed by XPS on the selected surfaces. It can be observed that all alloying elements are present in all conditions. In general the laser processes induced an increase of C pick-up from the atmosphere. The strong C content was attributed to absorption of C-containing organic molecules due to processing and handling in air. The atomic concentration of all alloying elements were found to be reduced after laser processing, however, they were present in all spectra. This was attributed to an extension of the surface oxide without a significant depletion in the alloying elements.

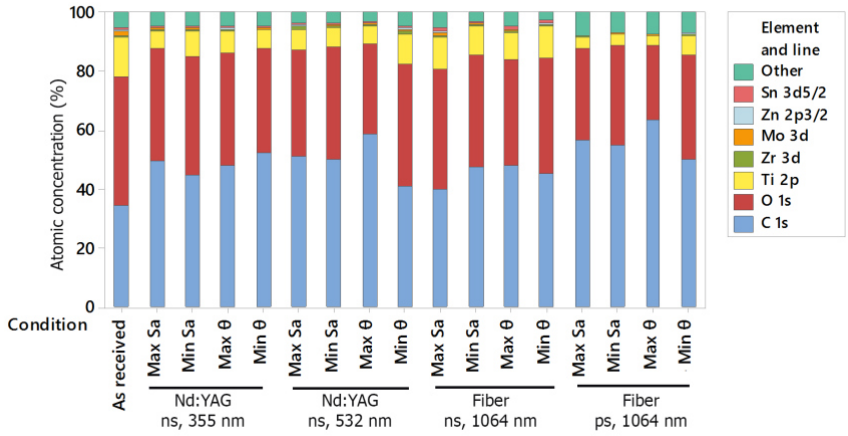

Figure 11. Summary of quantitative XPS on the representative conditions.

5. Process productivity

Process productivity can be calculated through as a function of machining rate (MR), which corresponds to the laser surface textured area over unit time. Machining rate, *MR,* can be calculated from

$$MR = \frac{A}{t_{cycle}} \tag{5}$$

where A is the textured area and t_{cycle} is cycle time that is required to complete the texture. For a simple rectangular geometry with l_1 and l_2 dimensions, cycle time, t_{cycle}, can be calculated with

$$t_{cycle} = \frac{l_1}{v} \cdot \left(\frac{l_2}{p} + 1\right) \tag{6}$$

The calculated *MR* values are shown in Figure 12. Evidently the high *PRR* systems with the use of scanner systems stand out for the high productivity. The use of linear stages can potentially provide a higher precision, however, for industrial applicability only small areas would be feasible. Indeed, Nd:YAG systems with higher PRR levels are available in the industry. Therefore, the results should be interpreted for matching the available textures provided by the low and high *PRR* sources with the productivity requirements of the application. A possible way to increase the productivity of the low *PRR* solutions is to use beam shaping strategies to split the highly energetic beam into several parts to carry out parallel machining. In order to match the *MR* of the high *PRR* systems, roughly 1000 beams should operate in parallel.

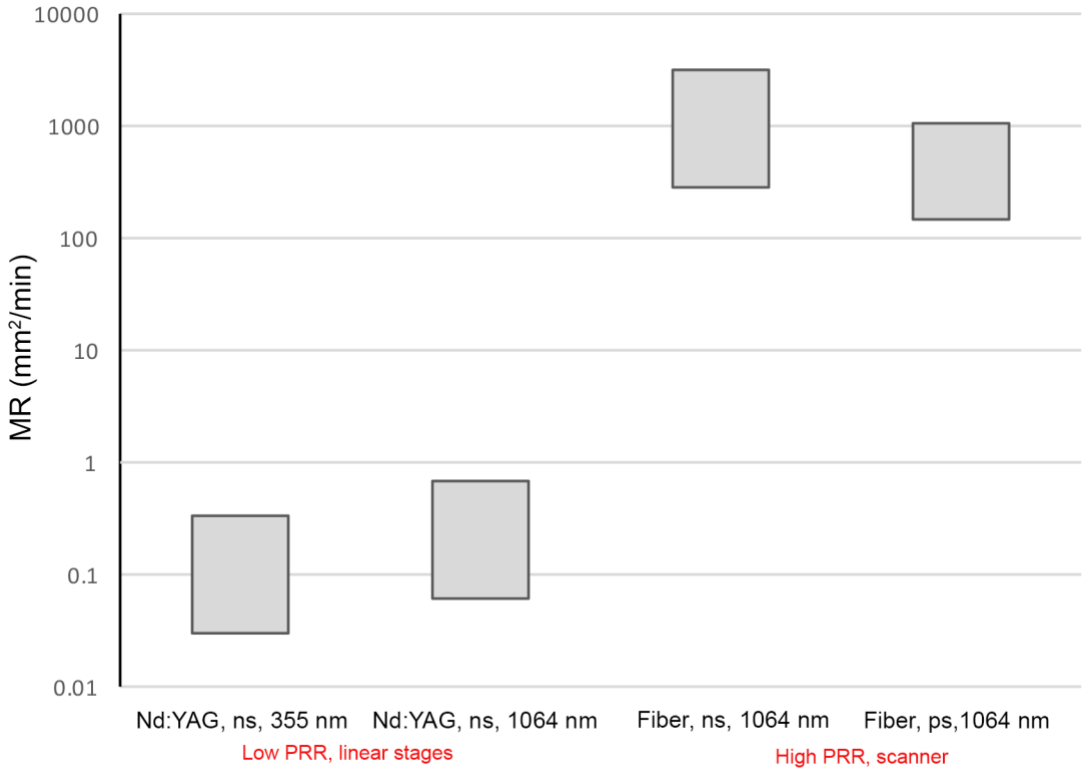

Figure 12. Machining rates of the tested configurations.

6. Possible allocation of the surface textures on an orthopaedic implant

The laser-induced surface patterns provided a so-called "catalogue of choices", which can be potentially assigned to different locations of femoral component of a total hip replacement implant. The main components as shown in Figure 13 along with the proposed surface structures. For ensuring good osseointegration with the acetabular cup and the femoral stem the highly rough and hydrophilic surfaces provided ns fiber laser are a good match. These treatments have shown to increase the α-phase content and potentially increase the elastic modulus. In this location and remaining only on the surface, such increase in the elastic modulus is not expected to be problematic. Meanwhile, the integrity of the surface due to the high amount of undercuts and oxidation should be assessed. Similar surfaces with higher water contact angles have been also found when the Nd:YAG source with the UV wavelength. The UV laser provides a less-invasive option by inducing periodic and shallow structures, which can also be exploited. The thermal damage is smaller, therefore excessive α-phase transformation. The relatively large area would require higher productivity. This point can be overcome by employing sources with similar wavelength and pulse duration with higher PRR. From this point of view, the

NIR Nd:YAG source does not provide any further advantage. The ps-pulsed fiber laser provides the LIPSS, which can be exploited on the femoral head and the femoral stem. This would likely enhance tribological and antibacterial properties [35,54].

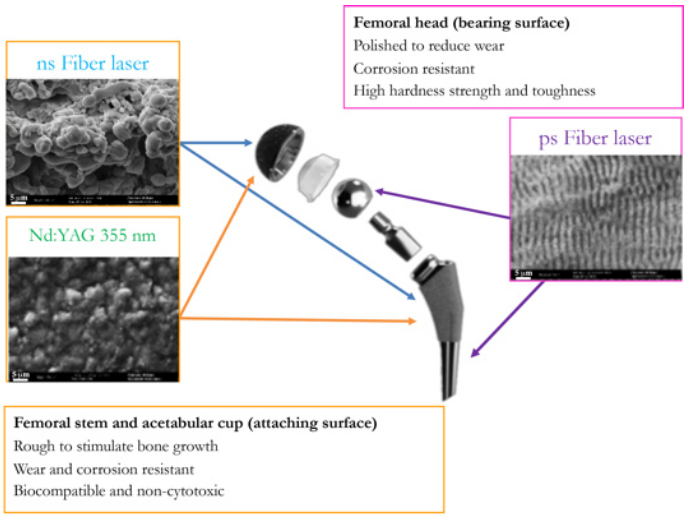

Figure 13. A possible allocation of different surface textures on a typical femoral component of a total hip replacement implant.

7. Conclusions

Laser surface texturing of a Ti-11.5Mo-6Zr-4.5Sn β-Ti alloy with 4 different industrial solid state lasers has been demonstrated. This way laser-material interaction employing ps to ns pulse durations with ultraviolet (UV) and near infrared (NIR) wavelengths could be also assessed. The obtained surface structures have been analysed for their surface topography, wetting properties, as well as chemistry. The main conclusions are:

(i) Laser material interaction was found to be dominated by melt generation and vaporization with the ns-pulses, whereas the so-called cold ablation with the low ps-pulses generated the laser induced periodic surface structures (LIPSS);

(ii) With the ns-pulsed lasers a significant difference due to the wavelength could not be observed concerning the material removal mechanisms; however, relatively longer duration and the high pulse repetition rat (*PRR*) of the ns-pulsed fiber laser proved to be important. With similar energy levels, the ns-pulsed fiber laser provided more material removal as well as a larger variety of surface textures compared to the ns-pulsed Nd:YAG laser;

(iii) Overall, the obtained surfaces were characterized with average roughness values between Sa=0.4 to 20 μm. While the areal surface roughness parameters are good indicator to the surface texture, they do not distinguish properly the LIPSS from the initial surface roughness and the influence of the undercuts formed in the highly rough surfaces;

(iv) The wetting behaviour of the obtained textures could be well-linked to the average surface roughness and the chemical composition of the surface. It is concluded that the high oxidation accompanied by the increased roughness provides a superhydrophobic surface on the β-Ti alloy;

(v) The surface texturing process can also induce phase changes on the β-Ti alloy. The conditions with the highest surface roughness obtained with the ns-pulsed fiber laser showed higher oxidation as well as significant α-phase transition. This is due to the fact that the alloy is solution treatable and the texturing process can induce such thermal conditions throughout the process;

(vi) The process productivity is highly dependent on the *PRR*. Both fiber and Nd:YAG sources today can operate at high PRR levels, however, the thermal accumulation should be also assessed; and

(vii) A tentative allocation of the obtained textures on a hip implant has been demonstrated. Potentially, the implants can be locally tailored to the required properties ranging from enhanced osseointegration, better friction behaviour, as well as antibacterial behaviour.

The work shows a systematic view of how the light-material interaction can be studied to modify surface topography and surface chemistry. The *in-vitro* and *in-vivo* assessment of the generated surfaces remain an open question. However, this work is expected to provide insights to design and choose the correct surface topography before extensive, labour-intensive, and costly biological studies.

Acknowledgements

The authors wish to express their gratitude to Mahr GbmH and CMF Marelli for their support with the surface metrology equipment.

References

[1] Dearnley PA. A Review of Metallic, Ceramic and Surface-Treated Metals used for Bearing Surfaces in Human Joint Replacements. Proc Inst Mech Eng Part H - J Eng Med. (1999)213(2):107–35.

[2] Long M, Rack H. Titanium alloys in total joint replacement—a materials science perspective. Biomaterials. (1998 Sep)19(18):1621–39.

[3] Ratner BD, Hoffman AS, Schoen FJ, Lemons JE. Biomaterials Science: An Introduction to Materials in Medicine. 3rd ed. Elsevier; (2013.).

[4] González JEG, Mirza-Rosca JC. Study of the corrosion behavior of titanium and some of its alloys for biomedical and dental implant applications. J Electroanal Chem. (1999)471(2):109–15.

[5] Cawley J, Metcalf JEP, Jones AH, Band TJ, Skupien DS. A tribological study of cobalt chromium molybdenum alloys used in metal-on-metal resurfacing hip arthroplasty. Wear. (2003)255(7–12):999–1006.

[6] Hiromoto S. Corrosion of Metallic Biomaterials in Cell Culture Environments. Electrochem Soc Interface. (2008)17(2):41–4.

[7] Lowenberg BF, Lugowski S, Chirman M, Davies JE. ASTM-F86 passivation increases trace element release from Ti6AI4V into culture medium. J Mater Sci Mater Med. (1994)5(6–7):467–72.

[8] Sumner R, Ph D, Galante J. Determinants of Stress Shielding: design versus materials versus interface. Clin Orthop Relat Res. (1992)274:202–12.

[9] Park CH, Park JW, Yeom JT, Chun YS, Lee CS. Enhanced mechanical compatibility of submicrocrystalline Ti-13Nb-13Zr alloy. Mater Sci Eng A. (2010)527(18–19):4914–9.

[10] Mohammed MT. Beta Titanium Alloys: The Lowest Elastic Modulus for Biomedical Applications: A Review. Int J Chem Nucl Metall Mater Eng. (2014)8(8):726–31.

[11] Demir AG, Previtali B, Lecis N. Development of laser dimpling strategies on TiN coatings for tribological applications with a highly energetic Q-switched fibre laser. Opt Laser Technol.

(2013)54:53–61.

[12] De Giorgi C, Furlan V, Demir AG, Tallarita E, Candiani G, Previtali B. Laser micropolishing of AISI 304 stainless steel surfaces for cleanability and bacteria removal capability. Appl Surf Sci. (2017)406.

[13] Furlan V, Biondi M, Demir AG, Pariani G, Previtali B, Bianco A. Sub-micrometric surface texturing of AZ31 Mg-alloy through two-beam direct laser interference patterning with a ns-pulsed green fiber laser. Appl Surf Sci. (2017)423.

[14] Waugh DG, Lawrence J, Brown EM. Osteoblast cell response to a CO2 laser modified polymeric material. Opt Lasers Eng. (2012 Feb)50(2):236–47.

[15] Chan CW, Hussain I, Waugh DG, Lawrence J, Man HC. Effect of laser treatment on the attachment and viability of mesenchymal stem cell responses on shape memory NiTi alloy. Mater Sci Eng C. (2014)42:254–63.

[16] Purnama A, Furlan V, Dessi D, Demir AG, Tolouei R, Paternoster C, et al. Laser surface texturing of SS316L for enhanced adhesion of HUVECs. Surf Eng. (2018)0(0):1–10.

[17] Brown MS, Arnold CB. Laser Precision Microfabrication. Sugioka K, Meunier M, Piqué A, editors. Berlin, Heidelberg: Springer Berlin Heidelberg; (2010.) 91-120 p. (Springer Series in Materials Science; vol. 135).

[18] Bandyopadhyay A, Balla VK, Roy M, Bose S. Laser surface modification of metallic biomaterials. Jom. (2011)63(6):94–9.

[19] Mirhosseini N, Crouse PL, Schmidth MJJ, Li L, Garrod D. Laser surface micro-texturing of Ti–6Al–4V substrates for improved cell integration. Appl Surf Sci. (2007 Jul)253(19):7738–43.

[20] Györgyey Á, Ungvári K, Kecskeméti G, Kopniczky J, Hopp B, Oszkó A, et al. Attachment and proliferation of human osteoblast-like cells (MG-63) on laser-ablated titanium implant material. Mater Sci Eng C. (2013 Oct)33(7):4251–9.

[21] LIU X, CHU P, DING C. Surface modification of titanium, titanium alloys, and related materials for

biomedical applications. Mater Sci Eng R Reports. (2004 Dec 24)47(3–4):49–121.

[22] Göransson A, Jansson E, Tengvall P, Wennerberg A. Bone formation after 4 weeks around blood-plasma-modified titanium implants with varying surface topographies: An in vivo study. Biomaterials. (2003)24(2):197–205.

[23] Lee T., Chang E, Yang C. Attachment and proliferation of neonatal rat calvarial osteoblasts on Ti6Al4V: effect of surface chemistries of the alloy. Biomaterials. (2004 Jan)25(1):23–32.

[24] Bagno A, Di Bello C. Surface treatments and roughness properties of Ti-based biomaterials. J Mater Sci Mater Med. (2004 Sep)15(9):935–49.

[25] Hao L, Lawrence J, Li L. Manipulation of the osteoblast response to a Ti-6Al-4V titanium alloy using a high power diode laser. Appl Surf Sci. (2005)247(1–4):602–6.

[26] Chen J, Ulerich JP, Abelev E, Fasasi A, Arnold CB, Soboyejo WO. An investigation of the initial attachment and orientation of osteoblast-like cells on laser grooved Ti-6Al-4V surfaces. Mater Sci Eng C. (2009)29(4):1442–52.

[27] Anselme K, Bigerelle M. Topography effects of pure titanium substrates on human osteoblast long-term adhesion. Acta Biomater. (2005)1(2):211–22.

[28] Hallgren C, Reimers H, Chakarov D, Gold J, Wennerberg A. An in vivo study of bone response to implants topographically modified by laser micromachining. Biomaterials. (2003)24(5):701–10.

[29] Brånemark R, Emanuelsson L, Palmquist A, Thomsen P. Bone response to laser-induced micro- and nano-size titanium surface features. Nanomedicine Nanotechnology, Biol Med. (2011 Apr)7(2):220–7.

[30] Hsiao WT, Chang HC, Nanci A, Durand R. Surface microtexturing of Ti-6Al-4V using an ultraviolet laser system. Mater Des. (2016)90:891–5.

[31] Coathup MJ, Blunn GW, Mirhosseini N, Erskine K, Liu Z, Garrod DR, et al. Controlled laser texturing of titanium results in reliable osteointegration. J Orthop Res. (2017)35(4):820–8.

[32] Chichkov B, Momma C, Nolte S. Femtosecond, picosecond and nanosecond laser ablation of solids. Appl Phys A. (1996)115:109–15.

[33] Reif J, Varlamova O, Costache F. Femtosecond laser induced nanostructure formation: self-organization control parameters. Appl Phys A. (2008 Jun 6)92(4):1019–24.

[34] Morgan R, Sutcliffe CJ, O'Neill W. Experimental investigation of nanosecond pulsed Nd:YAG laser re-melted pre-placed powder beds. Rapid Prototyp J. (2001)7(3):159–72.

[35] Bonse J, Koter R, Hartelt M, Spaltmann D, Pentzien S, Höhm S, et al. Tribological performance of femtosecond laser-induced periodic surface structures on titanium and a high toughness bearing steel. Appl Surf Sci. (2015)336:21–7.

[36] Cunha A, Elie AM, Plawinski L, Serro AP, Botelho Do Rego AM, Almeida A, et al. Femtosecond laser surface texturing of titanium as a method to reduce the adhesion of Staphylococcus aureus and biofilm formation. Appl Surf Sci. (2016)360:485–93.

[37] Jasim HA, Demir AG, Previtali B, Taha ZA. Process development and monitoring in stripping of a highly transparent polymeric paint with ns-pulsed fiber laser. Opt Laser Technol. (2017)93.

[38] Kietzig A-M, Hatzikiriakos SG, Englezos P. Patterned superhydrophobic metallic surfaces. Langmuir. (2009 Apr 21)25(8):4821–7.

[39] Ahmmed KMT, Ling EJY, Servio P, Kietzig A-M. Introducing a new optimization tool for femtosecond laser-induced surface texturing on titanium, stainless steel, aluminum and copper. Opt Lasers Eng. (2015)66:258–68.

[40] Furlan V, Demir AG, Previtali B. Micro and sub-micron surface structuring of AZ31 by laser re-melting and dimpling. Opt Laser Technol. (2015)75:164–72.

[41] Catchpole-Smith S, Aboulkhair N, Parry L, Tuck C, Ashcroft IA, Clare A. Fractal scan strategies for selective laser melting of 'unweldable' nickel superalloys. Addit Manuf. (2017)15:113–22.

[42] Buividas R, Mikutis M, Juodkazis S. Surface and bulk structuring of materials by ripples with long

and short laser pulses: Recent advances. Prog Quantum Electron. (2014 May)38(3):119–56.

[43] Biffi CA, Lecis N, Previtali B, Vedani M, Vimercati GM. Fiber laser microdrilling of titanium and its effect on material microstructure. Int J Adv Manuf Technol. (2010 Sep 7)54(1–4):149–60.

[44] Demir AG, Previtali B, Bestetti M. Removal of spatter by chemical etching after microdrilling with high productivity fiber laser. In: Physics Procedia. (2010.) p. 317–26.

[45] Demir AG, Pangovski K, O'Neill W, Previtali B. Laser micromachining of TiN coatings with variable pulse durations and shapes in ns regime. Surf Coatings Technol. (2014)258:240–8.

[46] Demir AG, Pangovski K, O'Neill W, Previtali B. Investigation of pulse shape characteristics on the laser ablation dynamics of TiN coatings in the ns regime. J Phys D Appl Phys. (2015 Jun 17)48(23):235202.

[47] Maressa P, Anodio L, Bernasconi A, Demir AG, Previtali B. Effect of surface texture on the adhesion performance of laser treated Ti6Al4V alloy. J Adhes. (2014)91(7):518–37.

[48] Demir AG, Previtali B, Bestetti M. Microvalve actuation with wettability conversion through darkness/UV application. J Micromechanics Microengineering. (2011)21(2).

[49] Waugh DG, Lawrence J, Langer N, Bidault S. Mixed-State Wetting and Wetting Transitions on Laser Surface Engineered Polymeric Materials. Int J Wettability Sci Technol. (2018)1:63–84.

[50] Lehr J, de Marchi F, Matus L, MacLeod J, Rosei F, Kietzig A-M. The influence of the gas environment on morphology and chemical composition of surfaces micro-machined with a femtosecond laser. Appl Surf Sci. (2014 Nov)320:455–65.

[51] Hashimoto K, Irie H, Fujishima A. TiO 2 Photocatalysis: A Historical Overview and Future Prospects. Jpn J Appl Phys. (2005 Dec 8)44(12):8269–85.

[52] Greenwood NN, Earnshaw A. Chemistry of Elements. Butterworth-Heinemann; 1997 p.

[53] Donadello S, Demir AG, Previtali B. Probing multipulse laser ablation by means of self-mixing interferometry. Appl Opt. (2018)57(25):7232–41.

[54] Rajab FH, Liauw CM, Benson PS, Li L, Whitehead KA. Production of hybrid macro/micro/nano surface structures on Ti6Al4V surfaces by picosecond laser surface texturing and their antifouling characteristics. Colloids Surfaces B Biointerfaces. (2017)160:688–96.

List of figures

List of tables